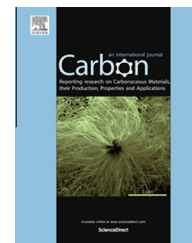


Available at www.sciencedirect.com

ScienceDirect

journal homepage: www.elsevier.com/locate/carbon

CVD grown CNTs within iron modified and graphitized carbon aerogel as durable oxygen reduction catalysts in acidic medium

Praveen Kolla ^a, Chuilin Lai ^a, Srujan Mishra ^b, Hao Fong ^{a,b,d}, Wendell Rhine ^c, Alevtina Smirnova ^{a,d,*}

^a Materials Engineering and Science PhD Program, South Dakota School of Mines & Technology, Rapid City, SD 57701, USA

^b Nano Science and Nano Engineering PhD Program, South Dakota School of Mines & Technology, Rapid City, SD 57701, USA

^c Aspen Aerogel Inc., Northborough, MA 01532, USA

^d Department of Chemistry and Applied Biological Sciences, South Dakota School of Mines & Technology, Rapid City, SD 57701, USA

ARTICLE INFO

Article history:

Received 19 March 2014

Accepted 7 August 2014

Available online 15 August 2014

ABSTRACT

CNTs were grown on iron-modified mesoporous graphitized carbon aerogel (GCA) at 700 °C, 800 °C and 900 °C using catalytic CVD method. Resultant CNT/GCA materials composition, morphology and structure were studied to understand their electrochemical stability and performance for oxygen reduction reaction (ORR) in acidic medium. CNT growth was increased from 700 °C to 800 °C, dominated by MWCNTs formation. In the temperature range from 800 °C to 900 °C, the growth was reduced by forming nanofiber/nanoribbon structures accompanied by MWCNTs. Mesoporosity of CNT/GCA composites declined at 700 °C and 800 °C due to MWCNT formation. However, CNT/GCA growth at 900 °C improved mesoporosity with substantial increase in pore volume (~3 times of GCA) due to formation of nanofibers and nanoribbons. The structure of CNT/GCA materials revealed nitrogen doping and dispersion of FeN_x phase. A synergistic contribution of CNT/GCA material structure and morphology to ORR activity was noticed. Among CNT/GCA materials, CNT-800 °C/GCA material showed ORR activity at lowest onset potential of 0.5 V. However, CNT-900 °C/GCA exhibits the highest ORR mass activity, with a half-wave onset potential difference of 120 mV with Pt (40 wt.%) / C. Moreover, CNT-900 °C/GCA demonstrates high selectivity (>3.97) to 4 electron ORR path, excellent methanol tolerance and electrochemical durability which makes it a potential DMFC cathode candidate.

Published by Elsevier Ltd.

1. Introduction

Polymer electrolyte membrane fuel cells such as Proton Exchange Membrane Fuel Cell (PEMFC) and Direct Methanol

Fuel Cell (DMFC) have potential to replace rechargeable batteries in portable electronic devices and automotive power sources [1]. Both types have a common oxygen reduction reaction (ORR) at the cathode where high noble metal (Pt)

* Corresponding author at: Department of Chemistry and Applied Biological Sciences, South Dakota School of Mines & Technology, Rapid City, SD 57701, USA. Fax: +1 605 394 1232.

E-mail address: Alevtina.Smirnova@sdsmt.edu (A. Smirnova).

<http://dx.doi.org/10.1016/j.carbon.2014.08.010>

0008-6223/Published by Elsevier Ltd.

loading is required to withstand slow ORR kinetics [2]. However, platinum exhibits mixed potentials due to methanol crossover from anode to cathode in DMFC which causes major voltage losses [3]. In order to make these fuel cells commercially viable, recent studies have focused to develop methanol tolerant ORR catalysts by studying platinum-transition metal (TM)-based alloys [4] and/or platinum-free ORR catalysts.

Among non-platinum ORR catalysts, TM-based [5] and impurity (heteroatom) doped carbon graphitic nanostructures [6] have shown significant ORR activity with onset potentials close to Pt/C catalysts. The observed ORR activity of TM-based catalysts was attributed to the presence of TM-N-C active sites. On other hand, due to breaking of electroneutrality of graphitic planes upon heteroatom doping in impurity doped carbon nanostructures creates positive charge on carbon that favors side-on O₂ surface adsorption. Additionally, these catalysts have shown better chemical stability in methanol, as they do not exhibit methanol oxidation at cathode in regard to methanol crossover problem associated with DMFC ORR catalysts. However, the activities and durability of these catalysts in acidic media are still insufficient due to acidic dissolution of TMs in TM-based ORR catalysts and corrosion of amorphous carbon in heteroatom doped graphitic structures. In this regard, development of low-cost carbon-based (platinum-free) methanol tolerant catalysts with platinum-like durability in acidic environment through easily scaled up methods will be a viable solution.

Alternatively, carbon aerogel materials have the advantage of high specific surface areas (SSAs) with interconnected 3D porous networks and good electrical conductivity [7]. In the past, (TMs) were impregnated into carbon aerogel matrix to exploit the unique advantage of their morphology and to induce structural changes for better catalytic performance [8,9]. Recent study on nitrogen-doped 3D iron-modified graphene aerogel material resulted in ORR catalytic activity close to Pt/C with low H₂O₂ yield, highlighting the importance of 3D-morphology and high SSA of the aerogel support [10]. In addition, iron-doped carbon aerogel was demonstrated lately [11,12] as porous substrate for direct growth of carbon nanotubes. However, the presence of graphitic shell surrounding TM prevents the growth of CNTs [11,13].

In this regard, we synthesized 3D-graphitized carbon aerogels (GCAs) by thermal treatment of iron-modified carbon aerogels [14]. The current study is focused on applying the 3D-GCA material as porous substrate for catalytic CVD growth of CNTs, and understanding catalytic growth of carbon nanostructures as a function of growth temperature. Despite the previous claim [11,13], the current study shows that CNT growth is not influenced by the presence of graphitic shell surrounding iron nanoparticles. In addition, graphitization of carbon aerogel prior to CNT growth plays a significant role in improving electrochemical stability along with methanol tolerance in acidic medium. Moreover, presence of CNTs within iron-doped GCA structure produced heteroatom/TM-C-N ORR active sites, caused by nitrogen impregnation.

2. Materials and methods

2.1. Synthesis

Mesoporous carbon aerogel form Aspen Aerogels® was impregnated with iron (10 and 15 wt.%) as a catalyst for graphitization by wet incipient method. The iron modified carbon aerogels were heat-treated at 900 °C, 1200 °C, and 1400 °C in argon. It was found that, the degree of graphitization was proportional to the concentration of iron phase and the ratio of iron to iron nitride phase in the heat-treated samples. In carbon aerogel sample with 15 wt.% of iron sintered at 1200 °C, mesoporosity in the range of 3–4 nm and microporosity (<2 nm) is significantly improved by graphitization, without affecting the carbon aerogels' initial mesoporosity. In this case of ~15 wt.% iron doped samples, uniformly distributed ~43.5 nm iron nanoparticles surrounded by graphene layers are present [14]. Further, graphitized carbon aerogels (GCAs) with the highest amount of graphitization (15 wt.% iron heat-treated at 1200 °C) was used as a substrate for CNT growth via catalytic CVD at growth temperatures of 700 °C, 800 °C and 900 °C. Reduction gas (10% H₂ + 90% Ar) with flow rate of 100 mL/min was purged through the samples with 10 °C/min ramp rate in order to reduce iron oxide phase to metallic iron. After reaching the growth temperatures, reduction gas was switched to carbon containing gas (1.6% H₂ + 2.5% C₂H₂ + 95.9% N₂) and maintained (at a flow rate of 100 mL/min) during CNTs growth for 30 min (Fig. 1).

2.2. Composition, morphology and structure characterization

To estimate the amount of carbon (CNT) deposited (Eq. (1)) in GCA materials at different growth temperatures, the total weight of the GCAs before and after the CNTs growth was measured using an analytical microbalance from Denver Instrument®, APX-100 with 0.1 mg deviation.

$$\text{Carbon deposited (\%)} = 100 \times \frac{m_t - m_c}{m_c} \quad (1)$$

where m_c and m_t were the mass of GCA substrate before and after CNT growth, respectively. The relative elemental compositions (in terms of weight percentage) of the materials were estimated with a Zeiss Supra 40VP variable-pressure field-emission SEM with an Oxford Instruments energy-dispersive X-ray analyzer. The elemental composition provided was obtained from spectra recorded in X-ray energy window of 0–10 keV and by averaging over five different spots (of size ~1–2 μm) of the samples. The scanning electron micrographs were recorded using an in-lens detector at 30kx magnification, under electron beam acceleration of 2 keV. Multi point Brunauer–Emmett–Teller (BET) and Barrett–Joyner–Halenda pore size distribution (BJH-PSD) were analyzed from the nitrogen adsorption–desorption isotherms at 77 K by means of an automated Gemini 2375 Instrument (Micromeritics Instrument Corp.). The degassing of the catalysts was conducted at 200 °C in N₂ for 1 h prior to the analysis. The BJH method was used to estimate the pore size distribution and cumulative

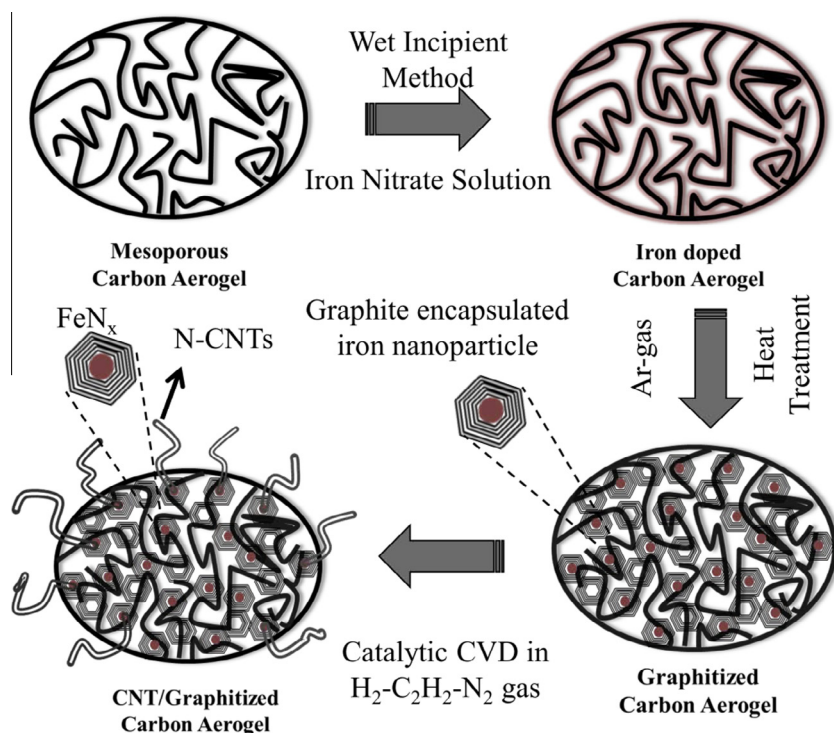


Fig. 1 – Material synthesis: Major steps in synthesis of iron modified 3D graphitized carbon aerogels (GCA) and CNT/GCA composites by catalytic CVD method. (A colour version of this figure can be viewed online.)

pore volume of pores ranging between 0 and 300 nm from the adsorption–desorption isotherms data.

Structure of the materials was characterized by a Rigaku Ultima Plus theta–theta X-ray diffractometer operated at 40 mA and 1.6 kW. Cu- $k\alpha$ radiation ($\lambda = 1.54178 \text{ \AA}$) was used to scan the materials from 10° to 90° (2θ) using a divergent slit with a scan rate of $0.667^\circ/\text{min}$. Raman spectroscopy was performed using Foster Freeman Micro-Raman spectrometer by illuminating sample with 532 nm laser beam. The catalyst material structure was further studied using high-resolution JEOL TEM-2100 transmission electron microscope (HRTEM), using an electron beam emitted from LaB₆ gun at 200 keV. For the TEM analysis, the catalyst powders were dispersed in methanol by sonication and placed on a square-mesh copper grid coated with carbon film (CF200-Cu).

2.3. Electrochemical studies

The electrochemical study of GCA and CNT/GCA materials was performed in analytical three-electrode half-cell configuration (RDE0018) from Princeton Applied Research, using 0.1 M HClO₄ electrolyte with an Ag/AgCl/0.1 M KCl reference electrode and Pt wire as a counter-electrode. The half-cell was connected to computer controlled setup from Pine Research Instrumentation[®] consisted of bi-potentiostat (AFCBP1), speed control unit (AFMSRCE) and E7R9-series Rotating Ring Disc Electrode (RRDE). The catalyst inks for RRDE measurements were prepared by sonicating 0.4 mL of 5% 1100 Nafion[™] solution in 20 mL of isopropanol and 79.6 mL of water with 0.6 g of the dry catalyst materials. Each of the catalyst inks was dispersed using Ultra Turrax[®]

homogenizer and 10 μL of the ink was deposited on glassy carbon electrode of 0.27 cm^2 surface area and dried to form a thin film. 2 μL of 5% Nafion[™] solution was added on the surface of catalyst to prevent the catalyst film from delamination during rotation experiments. Prior to the Cyclic Voltammetry (CV) experiment, the electrolyte was saturated with nitrogen by purging it through solution for 30 min followed by conditioning of the catalyst for 50 cycles between -0.5 V and 1.0 V at a scan rate of 50 mV/s . The redox reactions were studied by CV comparison in N₂- and O₂-saturated electrolyte and ORR kinetics was studied in O₂-saturated electrolyte at different RRDE rotation speeds from 100 to 2500 rpm by creating laminar flow of electrolyte in the electrochemical cell while Pt-ring was biased at 1.0 V at a scan rate of 5 mV/s from 1 to -0.2 V potential. The Pt/C catalyst (40 wt.% Pt HiSPEC 4100[™]) from Alpha Aesar[®] was used as a baseline for comparison of ORR selectivity to 4 electron transfer and mass activity.

3. Results and discussion

3.1. Composition

The percentage of carbon deposited on graphitized carbon aerogel (GCA) substrate after CNTs growth at 700°C , 800°C and 900°C is $\sim 63\%$, 117% and 86% , respectively. The relative elemental composition (wt.%) of GCA is compared with CNT/GCA grown at 700°C , 800°C and 900°C is presented in Table 1. Higher concentration of nitrogen in CNT/GCAs (2–3 wt.%) in comparison to GCA substrate indicates that nitrogen has been impregnated during CNT growth (Table 1). Previous studies on catalytic CVD growth of CNTs [15] also

Table 1 – EDS elemental composition: Relative elemental weight percent composition of graphitized carbon aerogel (GCA) and CNTs grown on GCA at 700 °C, 800 °C and 900 °C.

Material/composition	Carbon (C)	Iron (Fe)	Oxygen (O)	Nitrogen (N)
GCA	81.5 (± 0.6)%	15.2 (± 0.6)%	3.3 (± 0.2)%	0.5 (± 0.6)%
CNT/GCA-700 °C	87.0 (± 1.5)%	7.6 (± 0.5)%	2.0 (± 0.4)%	3.3 (± 1.6)%
CNT/GCA-800 °C	90.4 (± 1.3)%	5.4 (± 0.3)%	1.8 (± 0.3)%	2.4 (± 1.3)%
CNT/GCA-900 °C	87.8 (± 1.2)%	6.9 (± 0.4)%	2.6 (± 0.3)%	2.6 (± 1.2)%

emphasized development of nitrogen intercalated CNTs when nitrogen gas is used as an acetylene carrier gas. The percentage of CNTs deposited at different growth temperatures suggest that CNT yield on GCA substrate increases with temperature from 700 °C to 800 °C and slows down from 800 °C to 900 °C. This could be due to rapid diffusion of iron into GCA substrate at growth temperatures above 800 °C which hinders catalytic CNTs growth [16].

3.2. Morphology

3.2.1. Scanning electron microscopy

The scanning electron micrographs of CNT/GCA materials (Fig. 2) indicate 1–20 μm long CNTs (having diameters of $<0.1 \mu\text{m}$) along with 5–10 μm long nanostructures such as carbon nanofibers and/or nanoribbons with diameters $<0.3 \mu\text{m}$. Specifically, at 700 °C MWCNTs have the highest yield (Fig. 2A), while at 800 °C MWCNTs along with few nanofiber/nanoribbon structures are produced (Fig. 2B). At 900 °C, mostly nanofibers and/or nanoribbons with a small percentage of MWCNTs (Fig. 2C) are observed. The nanofibers/nanoribbons yield along with MWCNTs at 800 °C and 900 °C is probably due to formation of larger multi-facet iron particles. The nanofibers/nanoribbons would have developed due to acetylene decomposition on one facet while graphitic platelets precipitate on the other [17]. Presence of abundant hydrogen in precursor gas may have played a significant role in termination of graphene dangling bonds at the edge of stacked graphite platelets [18].

3.2.2. BET and BJH-pore size distribution

Nitrogen adsorption–desorption isotherms for GCA and CNT/GCA composites (Fig. 3), BJH pore size distribution (Fig. 3, inset), and their corresponding morphological parameters such as specific surface area (SSA), mesoporous SSA, pore volume and average pore size (in Table 2) are used to understand the morphological changes occurred during CNT growth. Both GCA and CNT/GCA composite materials show mesoporous behavior with type IV hysteresis. The GCA shows isotherm hysteresis (Fig. 3A) sharply starting at partial pressure (P/P_0) of 0.45, which is typical for graphene-type materials. Furthermore, PSD of GCA (Fig. 3A, inset) confirms mesoporosity in the range of 3–4 nm and 20–30 nm along with significant microporosity (in $<2 \text{ nm}$ range). However, mesoporosity (evident from mesoporous SSA values in Table 2) of CNT-700 °C/GCA is reduced in comparison to GCA, while microporosity of GCA remained unchanged. In the case of CNT-800 °C/GCA, the mesoporosity is further reduced and pore volume is increased compared to GCA material. The reduction in the

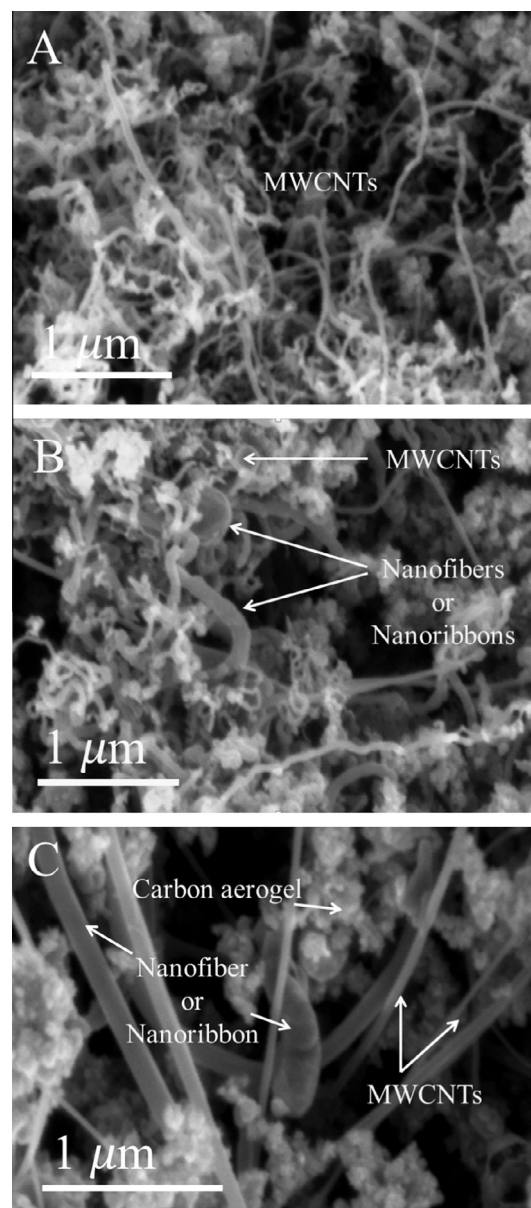


Fig. 2 – Scanning electron microscopy: Scanning electron micrographs of CNTs within GCA nanostructure grown at 700 °C (A), 800 °C (B) and 900 °C (C).

mesoporosity is due to presence of MWCNTs which have smaller intrinsic SSA compared to GCAs. The small improvement in pore volume might be due to development of graphitic-platelet structure associated with minor amount

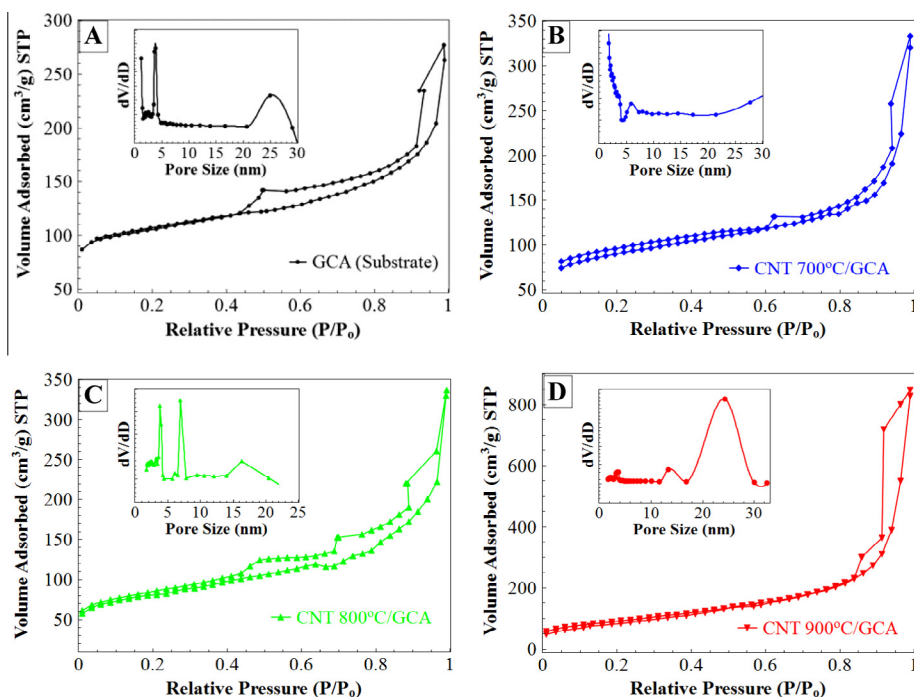


Fig. 3 – BET and BJH pore size distribution: Nitrogen adsorption–desorption isotherms of graphitized carbon aerogel substrate (A), and CNTs grown at 700 °C, 800 °C and 900 °C on graphitized carbon aerogel substrate (B), (C) and (D), respectively. Inset shows BJH mesoporous pore-size distribution of corresponding materials. (A colour version of this figure can be viewed online.)

Table 2 – Morphological parameters: Comparison of total specific surface area (SSA), mesoporous SSA, pore volume and average pore size parameters of graphitized carbon aerogel (GCA) with CNT/GCA materials grown at 700 °C, 800 °C and 900 °C.

Sample vs. properties	GCA	CNT 700 °C/GCA	CNT 800 °C/GCA	CNT 900 °C/GCA
Specific surface area (SSA) m ² /g	346	296	272	315
Mesoporous surface area (m ² /g)	232	121	46	310
Pore volume (cm ³ /g)	0.40	0.39	0.52	1.28
Average pore size (nm)	5.6	7.1	6.1	14.2

of nanofibers/nanoribbons and surface etching of amorphous carbon by hydrogen gas. Whereas in CNT-900 °C/GCA material, a significant mesoporosity improvement accompanied by enormous increase (~3 times of GCA) in pore volume is evident. This is due to excess yield of graphitic nanofibers and nanoribbons grown at 900 °C which might have greatly contributed to mesoporosity and pore-volume improvement [16].

3.3. Structure

3.3.1. XRD and Raman spectroscopy

X-ray diffraction spectra of GCA and CNT/GCAs, grown at 700 °C, 800 °C and 900 °C are compared in Fig. 4(A). The presence of iron oxide (Magnetite-Fe₃O₄) is confirmed by a small peak at 35.6° in graphitized carbon aerogel support (GCA). The absence of iron oxide peak at 35.6° in CNT/GCA materials indicates reduction of Iron oxide phase during CNT growth at temperatures ≥700 °C due to presence of hydrogen (H₂) gas in precursor gas mixture. Our previous study of Temperature Programmed Reduction (TPR) on GCA materials also indicated

reduction of Iron oxide phase completely to metallic iron in 10% H₂–90% Ar gas atmosphere [19]. Diffraction peaks of CNTs at 26° from (002) plane and 43° from (001) plane, iron metallic phase at 42.5°, 65° and 82.5° from (110), (200) and (211), and iron nitride (FeN_{0.049}, PDF#01-075-2128) complex at 43.46°, 50.63° and 74.41° from (111), (200) and (220) planes respectively, are present. It is possible that nitrogen atoms in low concentration can be incorporated into iron phase at temperatures of 1200 °C. The presence of CNT (100) peak at 43° in CNT/GCA composite and absence of the same peak in GCA confirms the formation of CNTs in CNT/GCAs. However, high relative peak intensity of graphitic (002) to CNTs (100) in CNT-900 °C/GCA compared to other CNT/GCA composites indicates low yield of CNTs and formation of graphitic nanofiber/nanoribbon structures at growth temperature of 900 °C. This phenomenon is also observed in SEM analysis (Fig. 2). The shift of CNT/GCAs (002) peaks to 26° with respect to graphitic (002) plane at 26.4° (dashed line), towards higher d-spacing confirms the presence of N-doping [20] which is also evident from EDS results (Table 1). In addition, iron nitride (220) peak

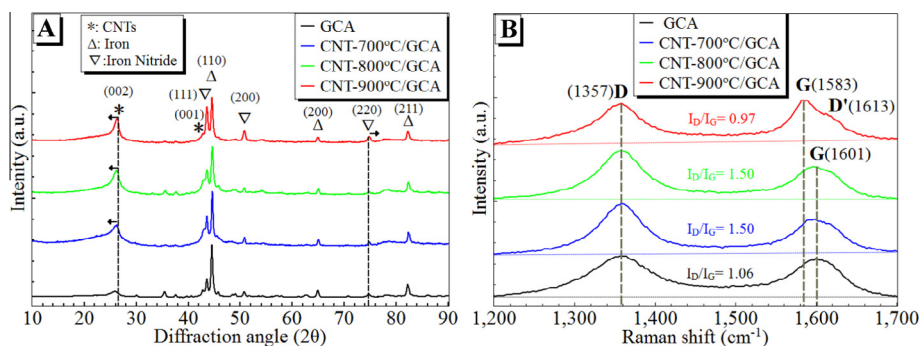


Fig. 4 – XRD and Raman spectroscopy: Comparison of X-ray diffraction data (A) and Raman spectra (B) of iron doped graphitized carbon aerogel (GCA) substrate (black) with CNTs grown on GCA at 700 °C, 800 °C and 900 °C (in blue, green and red, respectively). (A colour version of this figure can be viewed online.)

intensity for CNT-900 °C/GCA is higher and also shifted with respect to other CNT/GCA and GCA materials. This may be due to formation of excess iron nitride (FeN_x) phase, and structural changes occurred because of carbon incorporation into FeN_x phase by forming Fe-C-N structure at the highest growth temperature of 900 °C.

Raman spectra of GCA for CNT/GCA materials developed at growth temperatures of 700 °C, 800 °C and 900 °C are compared in Fig. 4B. Except CNT-900 °C/GCA material, all other materials show disordered defect mode (D) band at 1357 cm^{-1} and primary graphitic phonon (G) band at 1601 cm^{-1} . The G band originates from the tangential in-plane graphene carbon-carbon bond stretching while the D band arises due to structural defects induced by completely symmetric A_{1g} vibration of aromatic sp^2 -hybridized carbon rings. In the case of CNT/GCA materials grown at 700 °C and 800 °C, an increase in relative D to G band intensity ($I_D/I_G = 1.50$) compared to GCA material ($I_D/I_G = 1.06$) implies presence of nitrogen dopants and defects in CN_x nanotubes [21]. However, spectrum of CNT-900 °C/CGCA material shows down-shift in G band to 1583 cm^{-1} along with a shoulder corresponding to double resonance disordered (D') band centered at 1613 cm^{-1} . The split in the G band arises when the localized vibrational modes of impurities interact with extended phonon modes of graphene. However, D' band is induced by disorder and defects caused by randomly distributed impurities such as N-doping in CNTs and/or carbon atoms diffusion into FeN_x phase. G-band shift of 18 cm^{-1} towards lower energy in CNT-900 °C/GCA indicates charge transfer from nitrogen impurity atoms to carbon atoms [22]. Nevertheless, the D-band to G-band relative peak intensity of CNT-900 °C/GCA decrease ($I_D/I_G = 0.96$) which could be due to decrease in disorder and defect sites originated from excess graphitization of GCA support and/or graphene platelet stacking in the form of nanofibers/nanoribbons, surrounding iron particles at 900 °C.

3.3.2. Transmission electron microscopy

HRTEM analysis of GCA (Fig. 5A) reveals high degree of graphitization in vicinity of iron nanoparticles (inset, bottom of Fig. 5A), compared to the carbon aerogel material before graphitization (Fig. 1A, inset on left). A d -spacing of 0.34 nm

between graphene layers (inset, top of Fig. 5A) is observed in GCA, which is larger than the d -spacing of graphite (0.33 nm). The increase in GCA d -spacing is due to distortion in the stacking of graphene layers in the form of turbostratic structure [23]. TEM analysis of CNT-700 °C/GCA (Fig. 5B) reveals formation of MWCNTs with diameters in the range of $10\text{--}50\text{ nm}$. Most MWCNTs have open ends and very few show iron particles at the tips. The CNT growth via tip or base growth mechanism is influenced by interaction between iron particle and support at the growth temperature [24]. The MWCNTs having bamboo-type structure with compartments (Fig. 5B, inset) are evident which confirms nitrogen doping [25]. In CNT-800 °C/GCA material, MWCNTs with diameters in the range of $10\text{--}40\text{ nm}$ are present along with carbon nanofibers with diameters of $120\text{--}150\text{ nm}$ (Fig. 5C). Moreover, an improved d -spacing of 0.35 nm between graphene (002) planes in MWCNTs (Fig. 5C, inset) is observed. Improved d -spacing in CNT-800 °C/GCA could be due to impregnation of nitrogen and presence of surface functional groups developed during CNT growth. TEM image of CNT-900 °C/GCA shows the presence of carbon nanofibers (Fig. 5D) and nanoribbons (Fig. 5, inset on top) with diameters in the range of $100\text{--}200\text{ nm}$ along with complete graphitization (Fig. 5D, inset at the bottom) of GCA support. Coiled structure of nanofibers on both sides of iron particle is evident from TEM images of CNT/GCAs grown at 800 °C and 900 °C. Carbon nanoribbons having non-cylindrical cross-sections were confirmed by TEM analysis (Fig. 5D, inset on top). Formation of nanofibers and nanoribbons via CVD method in presence of transition metals such as Fe, Co, Ni and Cu in partial hydrogen environment along with carbonaceous gas have been reported in the temperature range of $500\text{--}1200\text{ °C}$ [26]. The coiled structure of nanofibers is formed due to stacking of small graphene layers from a multi-facet iron nanoparticle that are grown perpendicular to the fiber axis. The presence of hydrogen and nitrogen heteroatoms during the growth is useful in stabilizing the graphene layers that contain dangling bonds. Whereas, nanoribbons are due to growth of unrolled graphene layers formed from iron particle parallel to fibril axis. Similar nanoribbon structures were also noticed elsewhere [26] claiming that these structures have striking resemblance with MWCNTs due to the presence of particle at one end of the ribbon.

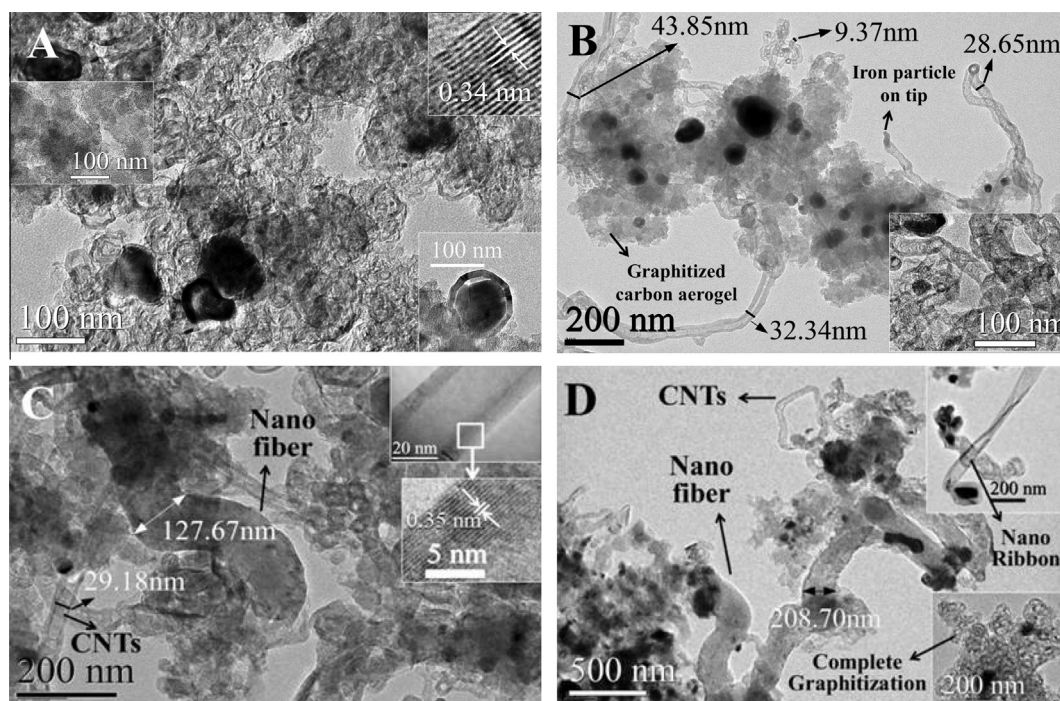


Fig. 5 – Transmission electron microscopy: HRTEM analysis of the iron nanoparticles impregnated graphitized carbon aerogels (A) and CNTs grown on GCA substrate at 700 °C, 800 °C and 900 °C in (B), (C) and (D), respectively.

3.4. Electrochemical behavior

3.4.1. Cyclic Voltammetry

To understand redox reactions and their relative qualitative ORR activity, Cyclic Voltammetry (CV) of GCA and CNT/GCA composites in N_2 - and O_2 -saturated electrolyte are compared (Fig. 6). GCA shows (Fig. 6A) redox peaks corresponding to transition of iron oxide phases ($Fe(III) \leftrightarrow Fe(II)$), at 0.33 and 0.37 V, respectively. However, the redox peaks decline with cycle number due to dissolution of iron oxide phase in electrolyte solution. The iron oxide redox peaks with similar behavior are also visible in CNT/GCAs grown at 700 °C and 800 °C. However, the relative magnitude of iron oxide redox peaks reduced due to decrease in iron oxide phase with growth temperature and disappeared completely in CNT-900 °C/GCA. The reduction of iron oxide phase in CNT/GCA with growth temperature is also apparent in XRD studies (Fig. 4A). The fall of iron oxide redox peaks in CNT/GCA with growth temperature could also be due to increase in surface coverage of iron oxide species by carbon nanostructures and/or formation of more chemically-stable form of iron phase.

CV comparison of GCA and CNT/GCAs in O_2 -saturated electrolyte reveals their relative oxygen reduction behavior. GCA and CNT-700 °C/GCA do not exhibit significant oxygen reduction behavior while CNT-800 °C/GCA and CNT-900 °C/GCA demonstrate higher oxygen reduction activity. However, among GCA and CNT/GCA materials, CNT-900 °C/GCA exhibits the highest ORR activity. Moreover, CVs of CNT-900 °C/GCA (Fig. 6D) show platinum-like hydrogen evolution and hydrogen oxidation behavior in reduction and oxidation cycles, respectively. This is due to the inverted elec-

trode setup and voltammogram scan range beyond hydrogen evolution-oxidation region. Hydrogen evolved in the reduction cycle below -0.3 V forms hydrogen gas bubbles and accumulates onto the working electrode surface (Fig. 6D, illustration below). In the corresponding oxidation cycle, the oxidation of hydrogen occurs by consuming hydrogen bubbles from the electrode surface (Fig. 6D, inset above) [27]. This behavior is absent (Fig. 6D, dark brown) when CV is obtained in -0.3 to 1.0 V range. The highest hydrogen evolution activity of CNT-900 °C/GCA among GCA and other CNT/GCAs suggest that CNT-900 °C/GCA has not only significant ORR activity, but also can be considered as potential candidate for Hydrogen Evolution Reaction (HER).

3.4.2. Oxygen reduction kinetics

To further understand ORR behavior and the reaction kinetics of the GCA and CNT/GCAs, polarizing currents from the disc electrode measured at 1600 RPM with 5 mV/s scan rate are compared with Pt/C catalyst (Fig. 7A). Corresponding ring currents (Fig. 7B, top), which is a direct measure of ORR byproduct peroxide ion oxidation, are also compared with Pt/C catalyst. Between GCA and CNT/GCA materials, CNT-900 °C/GCA shows high ORR activity at onset potential of 0.45 V compared to Pt/C catalyst (onset potential of 0.57 V). However, CNT-800 °C/GCA exhibits the lowest ORR onset potential of 0.50 V among all CNT/GCAs despite its lower mass activity in comparison to CNT-900 °C/GCA. The lowest onset potential displayed by CNT-800 °C/GCA could be due to its high amount of nitrogen doping evident from composition analysis. However, lower mesoporosity of CNT-800 °C/GCA in comparison to CNT-900 °C/GCA may reduce accessibility of ORR active

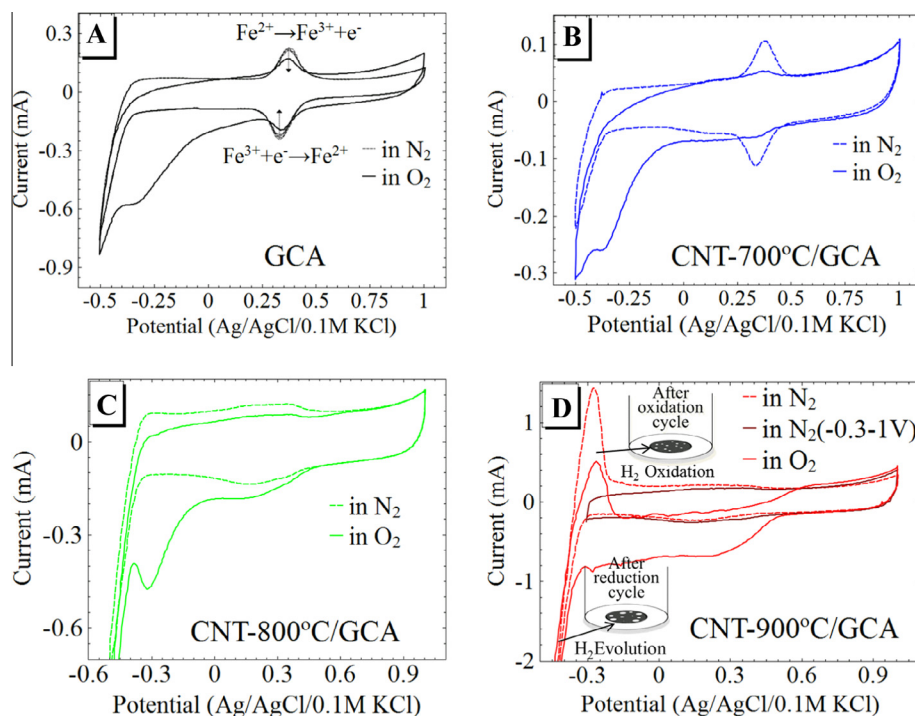


Fig. 6 – Cyclic Voltammetry (CV): CV comparison of GCA (A) and CNT/GCA materials (B, C and D, corresponding to growth temperatures of 700 °C, 800 °C and 900 °C, respectively) in N_2 - and O_2 -saturated 0.1 M HClO_4 electrolyte at a scan rate of 20 mV/s. (A colour version of this figure can be viewed online.)

sites. On the other hand, the highest ORR activity of CNT-900 °C/GCA can be due to a synergistic contribution from its improved mesoporosity and active ORR sites caused by nitrogen doping into graphenic carbon and/or change in iron nitride (FeN_x) structure. On the contrary, CNT-700 °C/GCA and GCA do not show realistic ORR activity, which is due to their mesoporosity collapse and absence of ORR active sites, respectively. The role of mesoporosity is crucial for the triple-phase boundary as average size of Nafion-ionomer is 20–40 nm and for the diffusion of chemical species of reactant and products [28].

To verify selectivity of GCA and CNT/GCA materials towards 4-electron transfer in ORR, electron transfer number (n) per each oxygen molecule during ORR as a function of applied potential is estimated (from Eq. (2)) and compared (Fig. 7B, bottom).

$$n = 4 \frac{I_d}{I_d + \frac{I_r}{N}} \quad (2)$$

where I_d is disc current, I_r is ring current and N (≈ 0.37) is the current collection efficiency of Pt ring. Comparison of GCA and CNT/GCA ring currents (Fig. 7B, top) and the calculated number of electrons (n) involved in ORR (Fig. 7B) are presented with respect to Pt/C catalyst. CNT-900 °C/GCA displays the lowest ring current while its electron transfer number (n) reaches that of Pt/C ($n = 3.96$ at 0.3 V) and surpasses Pt/C n -value at potentials higher than 0.1 V. Nevertheless, electron transfer numbers for GCA and other CNT/GCAs reach values ≥ 3.5 . The number of electrons transferred in CNT-900 °C/GCA material is also evaluated from Koutechy–Levich (K–L)

method by using diffusion limited ORR currents as a function of electrode rotating speeds (Fig. 7C). According to K–L approach, the number of transferred electrons (n) can be found by evaluating ' n ' from the slope of I^{-1} versus $\omega^{-1/2}$ plot by extrapolation of the following equation (Eq. (3)):

$$\frac{1}{I} = \frac{1}{I_k} + \frac{1}{B\omega^{1/2}} = \frac{1}{I_k} + \frac{1}{0.620 n F A D^{1/2} c \nu^{-1/2} \omega^{1/2}} \quad (3)$$

where I – measured current, I_k – O_2 reduction current free of mass transfer in the electrolyte solution, F – Faraday constant, 96,485, A – surface area of electrode (0.27 cm²), D – diffusion coefficient of the oxygen molecules (1.9×10^{-5} cm² s⁻¹), c – concentration (1.18×10^{-6} mol/cm³), ν – kinematic viscosity (9.87×10^{-3} cm²/s) and ω – rotation speed (rad/s) [29]. K–L plots for CNT-900 °C/GCA in the potential range of 0.0 V to -0.3 V (Fig. 7C) are linearly varying with rotation speed and the number of transferred electrons is varying in the range of 3.5–3.9. The linear relation between I^{-1} versus $\omega^{-1/2}$ indicates that rotation speeds are high enough and the reactants mass transport is limited by first-order diffusion process. The deviation of n values from RRDE and K–L method could be assigned to the unaccounted mass transport limitations within the bulk of the electrode.

3.4.3. Electrochemical stability and ORR mass activity

Chronoamperometry (CA) is used to evaluate CNTs-900 °C and Pt/C electrochemical stability and methanol tolerance in 1.0 M methanol added electrolyte solution (Fig. 8A). Initially, a drop in ORR activity for CNTs-900 °C is observed compared to Pt/C; however it stabilized after 1 h and showed

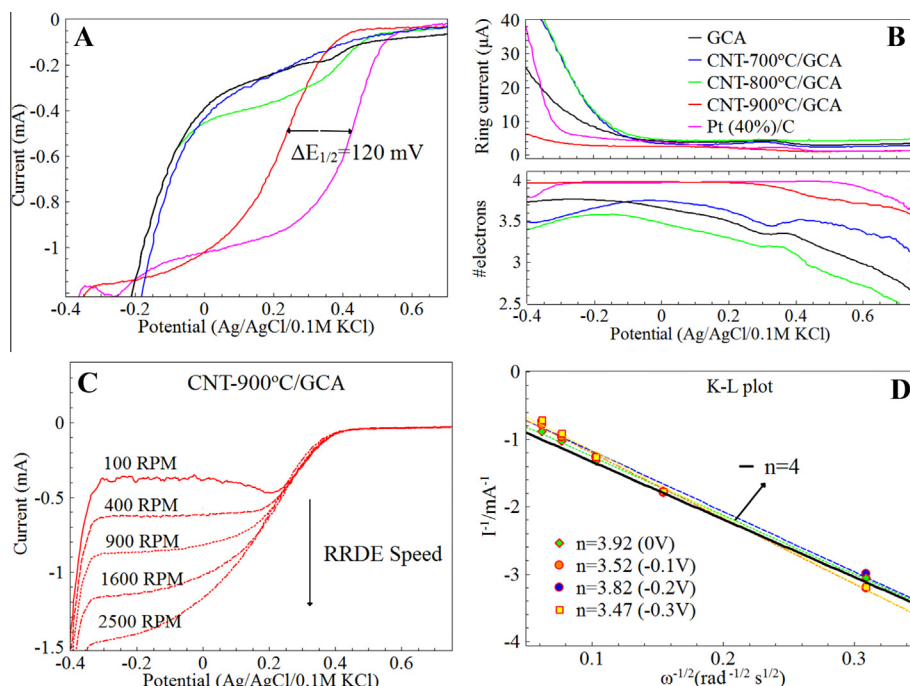


Fig. 7 – Oxygen reduction reaction (ORR) kinetics: Polarization currents of GCA, CNT/GCA and Pt (40 wt.)/C in O₂-saturated 0.1 M HClO₄ at a scan rate of 5 mV/s (A), their corresponding ring currents and the number of electrons involved per oxygen molecule during ORR estimated by RRDE technique (B), polarization currents of CNT-900 °C/GCA at different rotating speeds (C) and its corresponding number of electrons transferred during ORR at different potentials evaluated by K-L approach is presented with respect to $n = 4$, (D). (A colour version of this figure can be viewed online.)

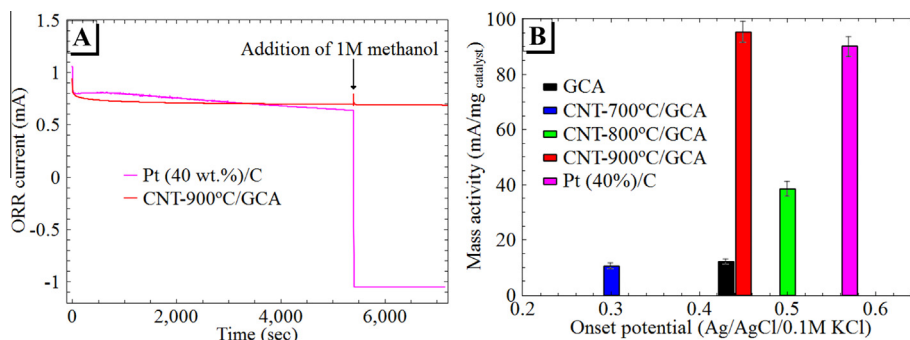


Fig. 8 – Chronoamperometry (CA) and ORR mass activity : CNT-900 °C and Pt/C materials durability and chemical stability in methanol evaluation using chronoamperometry at 0 V potential (A) and relative mass activity verses onset potentials for ORR of GCA and CNT/GCA materials in contrast to Pt/C catalyst (B). (A colour version of this figure can be viewed online.)

consistent ORR currents better than those of Pt/C. When methanol was added to the electrolyte, CNTs-900 °C material shortly recovered and exhibited constant ORR currents while Pt/C ORR currents suddenly dropped to negative values due to methanol oxidation/poisoning. Higher electrochemical stability and methanol tolerance of CNT-900 °C/GCA compared to Pt/C catalyst suggest that this catalyst can be considered as potential candidate for DMFC cathode. On the other hand, average kinetic mass activities of Pt/C, GCA and CNT/GCA materials evaluated (from Eq. (3)) at various disc rotation speeds are represented with respect to their corresponding ORR onset potentials. The ORR mass activity and ORR onset potentials of the materials compared follows the sequence: CNT-900 °C/GCA > CNT-

800 °C/GCA > GCA > CNT-700 °C/GCA and Pt/C > CNT-800 °C/GCA > CNT-900 °C/GCA > GCA > CNT-700 °C/GCA.

4. Conclusions

CNTs were successfully grown on the iron-modified mesoporous GCA substrate by catalytic CVD method at growth temperatures of 700 °C, 800 °C and 900 °C. Despite the previous claims, graphitization of carbon aerogel and presence of graphitic shell surrounding iron nanoparticles does not affect the CNT growth. Low partial pressure of acetylene in the precursor gas mixture (1.6% H₂ + 2.5% C₂H₂ + 95.9% N₂) at growth atmosphere might have improved the selectivity of CNT

growth. MWCNTs with diameters in the range 10–50 nm are yielded at all growth temperatures. Though there are few MWCNTs with iron particles at tips, the CNT growth is mostly dominated by the base-growth mechanism, which suggests a strong interaction between iron nanoparticles and GCA support. However, formation of nanofibers and nanoribbons at growth temperatures of 800 °C and 900 °C, and decrease in CNT growth at 900 °C was observed. Possible rapid diffusion of iron into GCA matrix yielding larger multi-facet iron particles at growth temperatures ≥ 800 °C might affect CNT yield by forming nanofiber/nanoribbon structures. The highest catalytic yield is observed for CNT-800 °C/GCA whereas significant structural and morphological changes occurred in CNT-900 °C/GCA. Nitrogen doping into CNTs is also evident in CNT/GCA composite material from EDS and structural analysis. BET and BJH-PSD studies reveal the loss of mesoporosity proportional to amount of CNTs growth at 700 °C and 800 °C. Mesoporosity and pore volume are significantly improved in CNT-900 °C/GCA materials due to formation of graphene platelet stacks in the form of nanofiber/nanoribbon structures and hydrogen etching of amorphous carbon deposited during CVD growth. The structural changes and higher dispersion in FeN_x phase are also evident in CNT-900 °C/GCA from XRD studies. Among CNT/GCA materials, CNT-800 °C/GCA showed the lowest ORR onset potential of 0.5 V, compared to 0.57 V for the state-of-art Pt/C catalyst. However, among CNT/GCA materials CNT-900 °C/GCA demonstrates the highest ORR mass activity of 95.2 mA/mg (at 0 V), with a half-wave onset potential difference of 120 mV with Pt/C catalyst. A synergistic improvement of CNT-900 °C/GCA in its structure and morphology has contributed to the highest ORR mass activity. In addition, the RRDE studies of GCA and CNT/GCAs reveal that ORR in CNT-900 °C/GCA is dominated by close to four-electron ($n = 3.96$ at 0.3 V) path, which shows lower peroxide yield than Pt/C. The CNT-900 °C/GCA also exhibits better electrochemical stability and methanol tolerance than Pt/C catalyst. Although observed ORR performance might originate from active sites created due to presence of nitrogen doping in carbon nanostructures and existence of FeN_x phase, our future studies will be focused on identifying specific ORR active sites and quantifying the relative site density in these materials. However, the role of carbon aerogel graphitization prior to CNT growth is confirmed to be significant in improving electrochemical stability in acidic medium. As for our knowledge, this is the first study that demonstrates ORR activity and electrochemical stability of CNTs grown on graphitized carbon aerogel substrate in acidic media.

Acknowledgements

This research was supported by the National Science Foundation (Grant No.: EPS-0903804), the National Aeronautics and Space Administration (Grant No.: NNX14AN22A), and the State of South Dakota. The authors would acknowledge Aspen Aerogel® for providing carbon aerogel samples.

Appendix A. Supplementary data

Supplementary data associated with this article can be found, in the online version, at <http://dx.doi.org/10.1016/j.carbon.2014.08.010>.

REFERENCES

- [1] Agnolucci P. Economics and market prospects of portable fuel cells. *Int J Hydrogen Energy* 2007;32:4319–28.
- [2] Nørskov JK, Rossmeisl J, Logadottir A, Lindqvist L, Kitchin JR, Bligaard T, et al. Origin of the overpotential for oxygen reduction at a fuel-cell cathode. *J Phys Chem B* 2004;108:17886–92.
- [3] Du CY, Zhao TS, Yang WW. Effect of methanol crossover on the cathode behavior of a DMFC: a half-cell investigation. *Electrochim Acta* 2007;52:5266–71.
- [4] Antolini E, Lopes T, Gonzalez ER. An overview of platinum-based catalysts as methanol-resistant oxygen reduction materials for direct methanol fuel cells. *J Alloys Compd* 2008;461:253–62.
- [5] Bezerra CWB, Zhang L, Lee K, Liu H, Marques ALB, Marques EP, et al. A review of Fe–N/C and Co–N/C catalysts for the oxygen reduction reaction. *Electrochim Acta* 2008;53:4937–51.
- [6] Yang Z, Nie H, Chen Xa, Chen X, Huang S. Recent progress in doped carbon nanomaterials as effective cathode catalysts for fuel cell oxygen reduction reaction. *J Power Sources* 2013;236:238–49.
- [7] Pekala RW. Organic aerogels from the polycondensation of resorcinol with formaldehyde. *J Mater Sci* 1989;24:3221–7.
- [8] Cotet LC, Baia M, Baia L, Popescu IC, Cosoveanu V, Indrea E, et al. Structural properties of some transition metal highly doped carbon aerogels. *J Alloys Compd* 2007;434–435:854–7.
- [9] Smirnova A, Wender T, Goberman D, Hu Y-L, Aindow M, Rhine W, et al. Modification of carbon aerogel supports for PEMFC catalysts. *Int J Hydrogen Energy* 2009;34:8992–7.
- [10] Wu Z-S, Yang S, Sun Y, Parvez K, Feng X, Müllen K. 3D Nitrogen-doped graphene aerogel-supported Fe₃O₄ nanoparticles as efficient electrocatalysts for the oxygen reduction reaction. *J Am Chem Soc* 2012;134:9082–5.
- [11] Steiner SA, Baumann TF, Kong J, Satcher JH, Dresselhaus MS. Iron-doped carbon aerogels: novel porous substrates for direct growth of carbon nanotubes. *Langmuir* 2007;23:5161–6.
- [12] Worsley MA, Stadermann M, Wang YM, Satcher Jr JH, Baumann TF. High surface area carbon aerogels as porous substrates for direct growth of carbon nanotubes. *Chem Commun* 2010;46:9253–5.
- [13] Fu R, Baumann TF, Cronin S, Dresselhaus G, Dresselhaus MS, Satcher JH. Formation of graphitic structures in cobalt- and nickel-doped carbon aerogels. *Langmuir* 2005;21:2647–51.
- [14] Kolla P, Kerce K, Zhao Y, Houk J, Normah Y, Rhine W et al. Iron modified graphitized carbon aerogels for sustainable energy applications. *MRS Online Proceedings Library* 2013; 1491: null–null.
- [15] Lee S-Y, Yamada M, Miyake M. Synthesis of carbon nanotubes over gold nanoparticle supported catalysts. *Carbon* 2005;43:2654–63.
- [16] Zhu S, Su C-H, Lehoczy SL, Muntele I, Ila D. Carbon nanotube growth on carbon fibers. *Diamond Relat Mater* 2003;12:1825–8.
- [17] Rodriguez NM, Chambers A, Baker RTK. Catalytic engineering of carbon nanostructures. *Langmuir* 1995;11:3862–6.

- [18] Nolan PE, Lynch DC, Cutler AH. Carbon deposition and hydrocarbon formation on group VIII metal catalysts. *J Phys Chem B* 1998;102:4165–75.
- [19] Kolla P, Kerce K, Normah Y, Houk J, Rhine W, Dixon D, et al. 3D-Graphitized and iron modified carbon aerogels for sustainable energy applications. *ECS Trans* 2013;50:1277–86.
- [20] Van Khai T, Na HG, Kwak DS, Kwon YJ, Ham H, Shim KB, et al. Significant enhancement of blue emission and electrical conductivity of N-doped graphene. *J Mater Chem* 2012;22:17992–8003.
- [21] Lim SH, Elim HI, Gao XY, Wee ATS, Ji W, Lee JY, et al. Electronic and optical properties of nitrogen-doped multiwalled carbon nanotubes. *Phys Rev B* 2006;73:045402.
- [22] Chiu PW, Duesberg GS, Dettlaff-Weglikowska U, Roth S. Interconnection of carbon nanotubes by chemical functionalization. *Appl Phys Lett* 2002;80:3811–3.
- [23] Sevilla M, Sanchís C, Valdés-Solís T, Morallón E, Fuertes AB. Direct synthesis of graphitic carbon nanostructures from saccharides and their use as electrocatalytic supports. *Carbon* 2008;46:931–9.
- [24] Kumar M, Ando Y. Chemical vapor deposition of carbon nanotubes: a review on growth mechanism and mass production. *J Nanosci Nanotechnol* 2010;10:3739–58.
- [25] Yadav R, Dobal P, Shripathi T, Katiyar R, Srivastava O. Effect of growth temperature on bamboo-shaped carbon–nitrogen (C–N) nanotubes synthesized using ferrocene acetonitrile precursor. *Nanoscale Res Lett* 2008;4:197–203.
- [26] Martin-Gullon I, Vera J, Conesa JA, González JL, Merino C. Differences between carbon nanofibers produced using Fe and Ni catalysts in a floating catalyst reactor. *Carbon* 2006;44:1572–80.
- [27] Nakabayashi S, Shinozaki R, Senda Y, Yoshikawa HY. Hydrogen nanobubble at normal hydrogen electrode. *J Phys: Condens Matter* 2013;25:184008.
- [28] Antolini E. Carbon supports for low-temperature fuel cell catalysts. *Appl Catal B* 2009;88:1–24.
- [29] Maruyama J, Abe I. Application of conventional activated carbon loaded with dispersed Pt to PEFC catalyst layer. *Electrochim Acta* 2003;48:1443–50.